Int. J. Electrochem. Sci., 9 **(2014)** 7935 - 7947

International Journal of
ELECTROCHEMICAL
SCIENCE
www.electrochemsci.org

Oxidation of Fe_3N for a High-Energy-Density Anode in Lithium Ion Batteries

Chang-Wei Su[1,2,*], *Lin-Xing Zhou*[1,2], *Jun-Min Li*[1,2,], *Meng-Chao Ye*[1,2], *Jun-Ming Guo*[1,2,†]

[1] Key Laboratory of Chemistry in Ethnic Medicinal Resources, State Ethnic Affairs Commission & Ministry of Education, Yunnan Minzu University, D-306, Guang-Jing Compound, Kunming 650500, PR China
[2] Engineering Research Center of Biopolymer Functional Materials of Yunnan, Yunnan Minzu University, Kunming 650500, PR China
[*]E-mail: abrastein@163.com; [†]E-mail: guojunming@tsinghua.org.cn.

Received: 23 September 2014 / *Accepted:* 20 October 2014 / *Published:* 28 October 2014

In this work, the oxidation behaviors of Fe_3N with micro-polygonal structures are studied in detail. At 300 ^oC, its micro-polygonal structures can be well retained, although the oxidation of Fe_3N has taken place. The oxidation product should be composed of Fe_3O_4 and Fe_2O_3 according to all XRD data for samples oxidized in different temperatures from 300 to 500 ^oC. The electrochemical properties of Fe_3O_4-Fe_2O_3 on Fe_3N are analyzed by conventional electrochemical technologies, containing discharge/charge analysis, cyclic voltammogram (CV) and electrochemical impedance spectroscopy (EIS). The results indicate that the Fe_3N-O-300 sample oxidized at 300 ^oC exhibits an extraordinary capacity retention and good rate performance with Columbic efficiency nearly 100%. The interface between Fe_3O_4-Fe_2O_3 and Fe_3N is confirmed by EIS with two depressed semicircles.

Keywords: Oxidation; Fe_3N; High-energy-density; Electrochemical properties; Lithium ion batteries.

1. INTRODUCTION

High-energy-density materials that undergo conversion reactions hold promise for next-generation lithium ion batteries [1]. For example, Fe_3O_4 possesses a high theoretical specific capacity of 926 mA h g^{-1} and undergoes a following conversion reaction [2].

$Fe_3O_4 + 8\ Li^+ + 8\ e \rightarrow 8\ Fe + 4\ Li_2O$ (1)

However, their practical applications are inhibited by serious capacity attenuation, which results from volume change of the materials during charge/discharge processes [3-5]. Forming nanostructures [6-11] (such as nanopore, nanopillar, nanofiber and nanorod) and/or composites with

carbon materials [12-19] (such as porous carbon, carbon nanotube and graphene) are two efficient strategies to suppress capacity attenuation. Alternatively, utilizing the interface between two compounds may be another simple and efficient method. For example, a shell@core structured Fe_3O_4@Fe_3N nanoparticle exhibited an improved electrochemical performance [20].

In this work, a Fe_3O_4-Fe_2O_3 and Fe_3N interface was constructed by direct oxidation of Fe_3N foils in hot air, and it has demonstrated that such an interface indeed improve the capacity retention of the cheap iron-oxide materials.

2. EXPERIMENTAL

2.1 Preparation of Fe_3N foils

Fe foils, which possess polygonal crystals with microns size, were fabricated by electrodeposition according to the reference [21]. Then, the electrodeposited Fe foils were cut into disks with a diameter of 1.6 cm (~2.0 cm^2).

To convert into Fe_3N foils, six Fe disks together with 1 g urea were put into a pipe stove (~ 2.5 L), then were annealed at 550 ^oC for 2 h in an atmosphere of N_2, and lastly were taken out after cooling to room temperature.

2.2 Oxidation of Fe_3N foils

The resultant Fe_3N disks were sintered for several hours in air atmosphere at 300 ^oC, 350 ^oC, 400 ^oC and 500 ^oC, respectively. For comparison, the Fe disks were also oxidized under above conditions. The weight increment of Fe_3N disks after oxidation was analyzed by a semimicro balance (readability: 0.01 mg, Mettler Toledo, MS105DU).

2.3 Characterizations

The morphologies of all samples were investigated by scanning electron microscopy (SEM, QUANTA 200, America FEI). Their X-ray diffraction (XRD) patterns were recorded using a D/max-TTRIII diffractometer with Cu Kα radiation over 2 θ range of 10 °−90 °.

2.4 Electrochemical measurements

Galvanostatic discharge/charge measurements were carried out in CR2025 coin cells using the Land battery system (CT2001) with a potential window of 3.0−0.1 V v.s. Li^+/Li. Cells were assembled in a high-purity argon-filled glovebox (Mikrouna, Super 1220/750). The oxidized Fe and Fe_3N disks were directly used as working electrode without any polymer binder. Lithium foils were used as both counter and reference electrodes, and Celgard 2320 was used as separator membrane. The electrolyte

was 1 M $LiPF_6$ in ethylene carbonate (EC) and dimethyl carbonate (DMC) (1:1 by volume). Cyclic voltammogram (CV) measurements were performed with an electrochemical workstation (CHI 604D, Shanghai Chenhua) at a scanning rate of 0.5 mV/s. Electrochemical impedance spectroscopy (EIS) was recorded between 100 kHz to 10 mHz with an amplitude of 5 mV under an open circuit voltage.

3. RESULTS AND DISCUSSION

3.1 Nitridation of the electrodeposited Fe disk

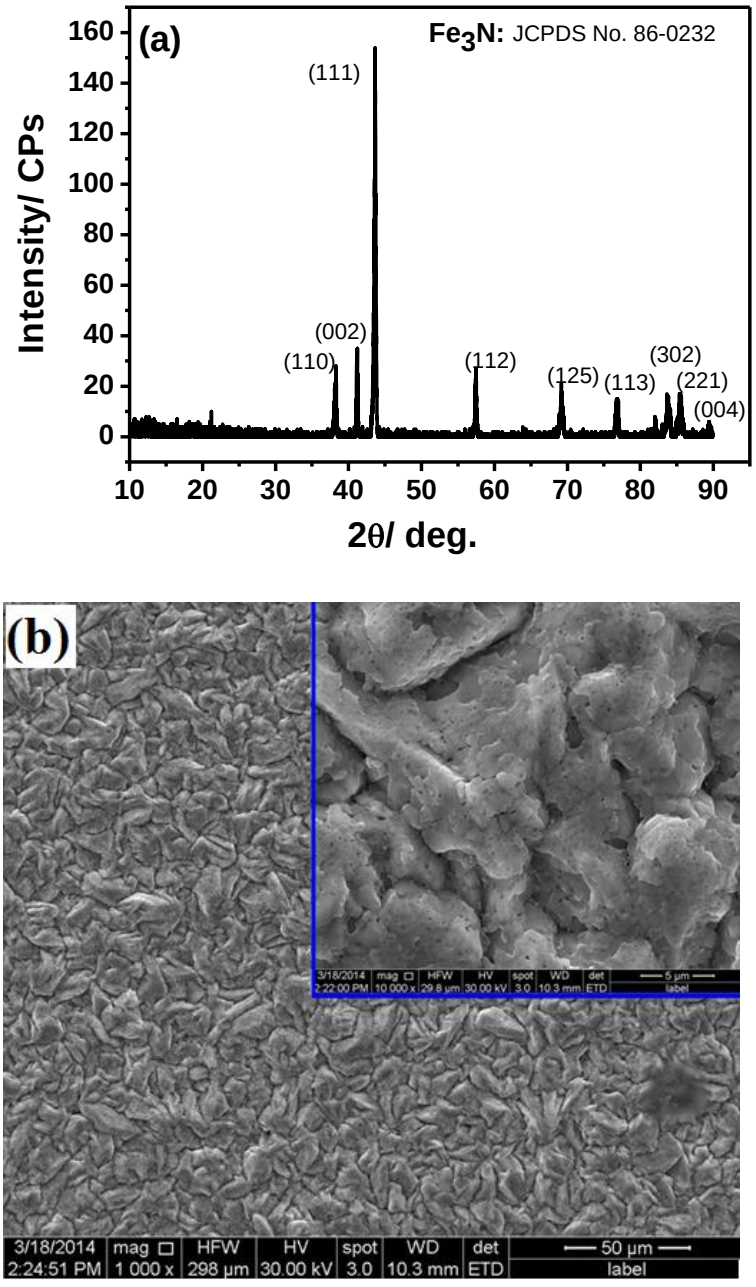

Figure 1. (a) XRD pattern and (b) SEM image of a nitrided Fe disk

The nitridation of a transition metal requires the presence of active nitrogen atoms. NH_3 that decomposed from the urea at a high surrounding temperature can provide active nitrogen atoms according to the following reaction,

$2\ NH_3 + Fe \rightarrow 2\ N^* + Fe + 3\ H_2$ (2)

where, Fe takes a role of catalyzer. Then active nitrogen atoms penetrate into the Fe crystals and the resultant is a nitride according to the following reaction,

$N^* + x\ Fe \rightarrow Fe_xN$ (3)

Fig. 1 shows the XRD pattern and the SEM image of the nitride. As shown in Fig. 1 a, the diffraction peaks coincide with those from a hexagonal structure of Fe_3N (JCPDS No. 86-0232). The Fe diffraction peaks disappear, indicating enough Fe_3N to be converted into. From Fig. 1 b, it can be obviously seen that the polygonal structures of Fe crystals are retained after nitridation. However, in the inset with high magnification shown in Fig. 1 b, there are many pinholes in the Fe crystals. These pinholes may be some channels, by means of which nitrogen atoms are transported to the inner of Fe crystals.

3.2 Oxidation of Fe_3N

The weight increments (Δm) of Fe_3N disks (Φ 1.6 cm, ~ 2.0 cm^2) changing with temperature and time are shown in Fig. 2. Below ~ 450 ^oC, the oxidation rate of Fe_3N is faster than that of Fe (see Fig. 2 a). At 300 ^oC, the oxidation of Fe and Fe_3N had also taken place. It can be seen from Fig. 2 b that for Fe_3N the value of Δm over 8 h is close to a constant, while for Fe the Δm value increases slowly.

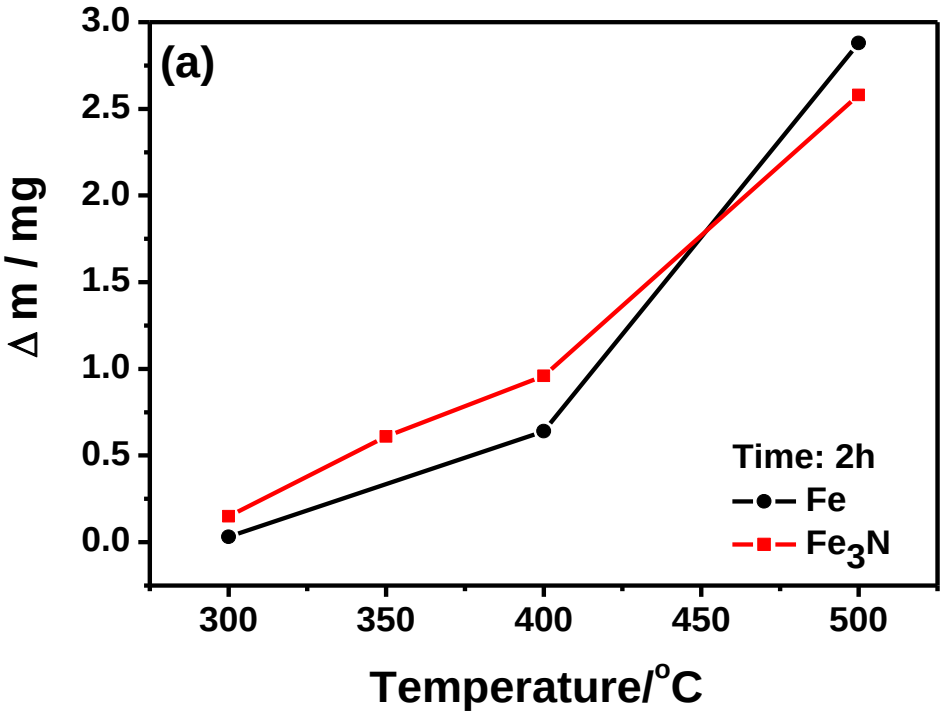

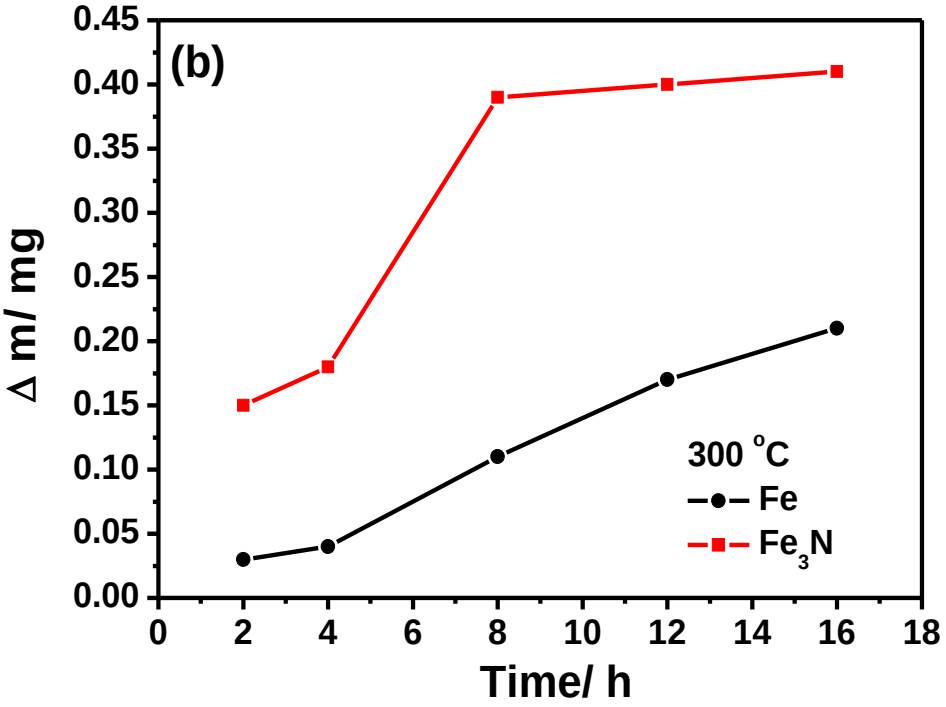

Figure 2. The relationships of (a) Δ m and temperature, (b) Δ m and time

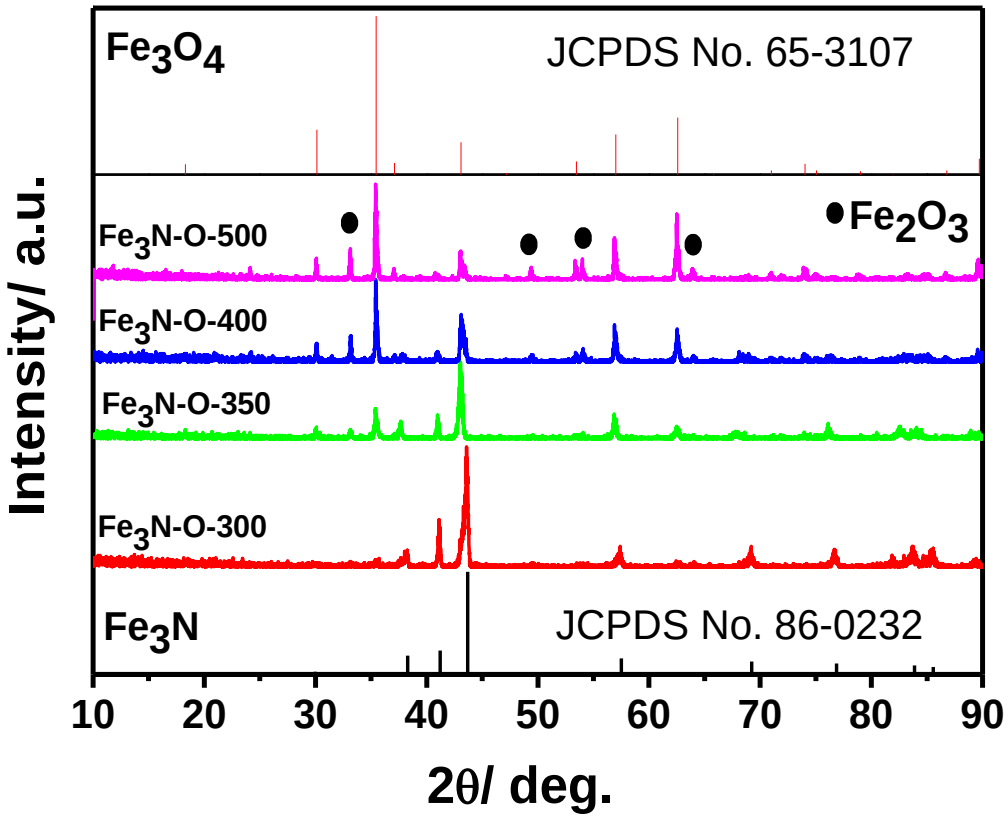

Figure 3. XRD patterns of four samples: Fe_3N-O-300, Fe_3N-O-350, Fe_3N-O-400 and Fe_3N-O-500

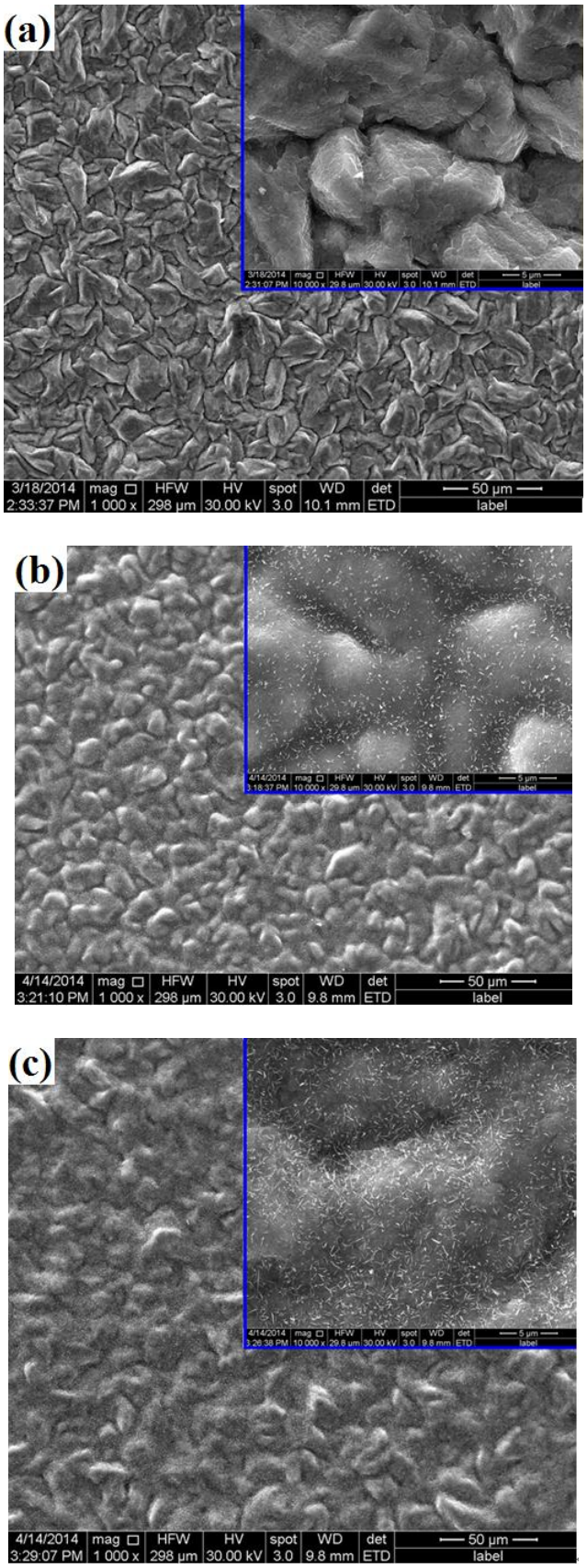

Figure 4. SEM images of (a) Fe_3N-O-300, (b) Fe_3N-O-350, and (c) Fe_3N-O-400

The sample of Fe_3N oxidized at 300 ^oC for 8 h marked Fe_3N-O-300, and the samples oxidized for 2 h at 350 ^oC, 400 ^oC and 500 ^oC marked Fe_3N-O-350, Fe_3N-O-400 and Fe_3N-O-500, respectively. Their XRD patterns are shown in Fig. 3. At 300 ^oC, the oxidation product of Fe_3N is main Fe_3O_4 according to two weak diffraction peaks, at 2 θ = 35.45 ^{o} and 62.57 ^{o}, which are the two characteristic strong peaks of Fe_3O_4 (JCPDS No. 65-3107). The two peaks become strong with the increase of sinter temperature, indicating more Fe_3O_4 were formed. However, it can be clearly seen that four diffraction peaks located 2 θ = 33.15 ^{o}, 49.48 ^{o}, 54.01 ^{o} and 63.99 ^{o} can be assigned to these of Fe_2O_3 (JCPDS No. 33-0664).

Fig. 4 shows SEM images of Fe_3N oxidized at different temperatures. The polygonal crystal shape is still retained after oxidation at 300 ^oC, however the pinholes in Fe crystals disappear (see the inset in Fig. 4 a). The result implies that the oxidation products of Fe_3O_4 and Fe_2O_3 with bigger volume fill pinholes up. Over 300 ^oC, the crystal shape changes and the crystal boundaries become illegible. Moreover, many glass-like splinters appear. It can be observed from Fig. 4 b and c that the numbers as well as the size of the splinters grow as the sintered temperature increases, implying that there is a nucleation growth process during the transformation of Fe_3N to Fe_3O_4-Fe_2O_3.

3.3. Electrochemical Performances

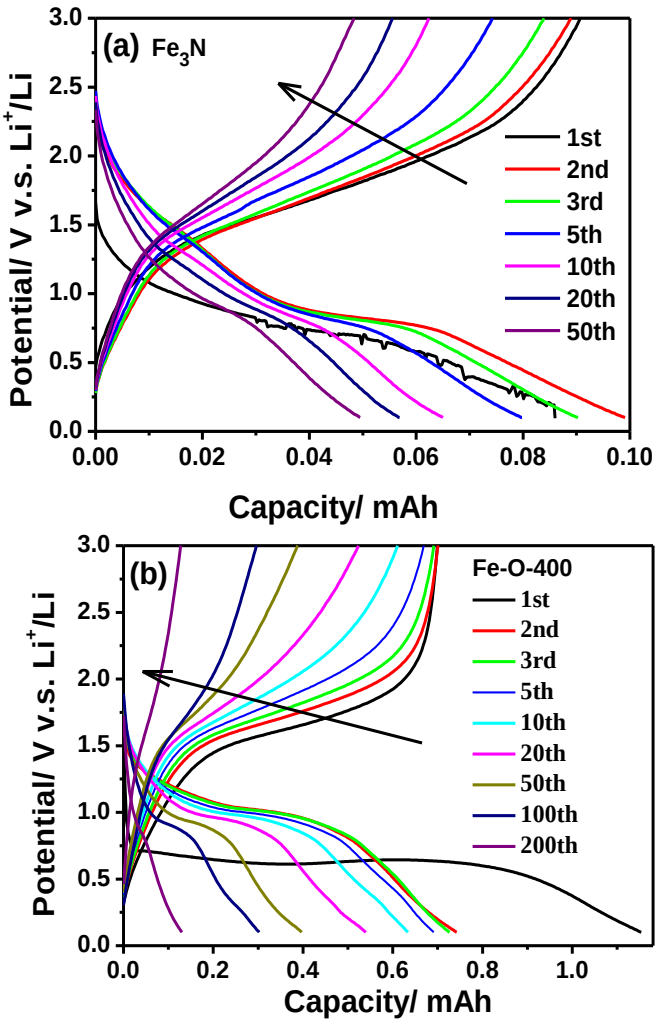

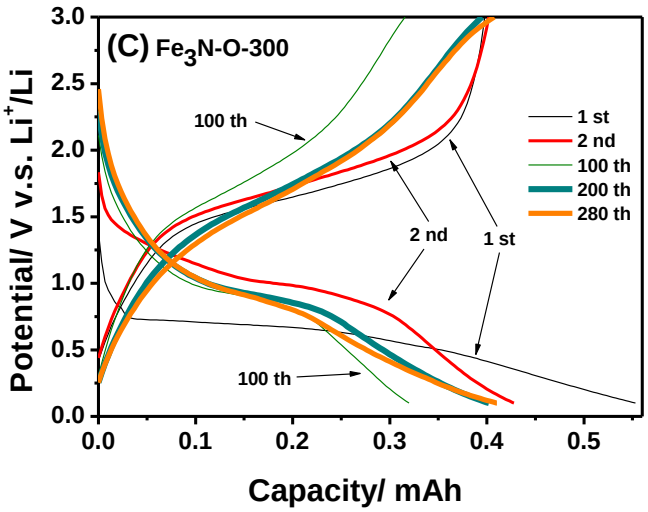

Figure 5. Discharge-charge voltage profiles of (a) Fe_3N, (b) Fe-O-400 and (c) Fe_3N-O-300

Fig. 5 shows the discharge-charge voltage profiles of the Fe_3N, Fe-O-400 (Fe disks oxidized at 400 ^oC) and Fe_3N-O-300 at 0.2 mA in the range of 0.1−3.00 V. The Fe-O-400 was selected, because the Δ m of Fe disks at 300 ^oC is few. As shown in Fig. 5 a, the nitriding material of Fe_3N exhibits a very low and attenuating capacity (< 0.1 mA h, ~10 mA h g^{-1}), while the Fe_3N, which was deposited by pulsed laser ablation of iron combined with N_2 gas DC discharge, exhibited a reversible discharge capacity of over 300 mA h g^{-1} [22]. A possible reason is that the nitriding layer is too dense to insert Li^+ ions into and the Fe_3N on the surface layer is only taking effect. Rapid capacity attenuation can be observed from Fig. 5 b, indicating that the interface of Fe and iron oxides is ineffective to improve their capacity retention. Interestingly, the capacity retention can be remarkably improved in the interface of Fe_3O_4-Fe_2O_3/Fe_3N as shown in Fig. 5 c, although the beginning several voltage profiles are the same as these of Fe-O-400. For example, a voltage plateau at 0.75 V followed by a sloping curve is exhibited in the first discharge, while it shifts to 0.98 V in subsequent discharge processes. And serious capacity degeneration in the second discharge process is also observed, which could be associated with the formation of a solid electrolyte interface (SEI) layer on the surface of the electrode. It is worth noting that the charge-discharge capacities of the 200th to 280th cycles are close to that of 2nd cycle, indicating an extraordinary capacity retention and cyclic behavior of the Fe_3O_4-Fe_2O_3/Fe_3N interface.

The durability of the Fe_3N-O-300 sample was estimated by cycling in the range of 0.1−3.00 V at stepwise current rates from 0.2 to 1.2 mA, then stepwise back to 0.2 mA for 200 cycles, lastly again stepwise current rates. It is clearly seen from Fig. 6 that the Fe_3N-O-300 sample exhibits extraordinary capacity retention with Columbic efficiency nearly 100%. After 350 cycling at different currents, the sample can still release a capacity of 0.41 mA h at the current of 0.2 mA, which is 83.67 % that of the second discharge capacity (0.49 mA h). From the 80th to 260th cycle at 0.2 mA, it is observed that the discharge/charge capacities rise with cycling. The capacity increasing phenomenon has been observed by other researchers on the interface of carbon/iron oxide [23, 24]. The cell exhibits also good rate performance, for example, still delivering 0.18 mA h at 1.2 mA (spending about 6 min).

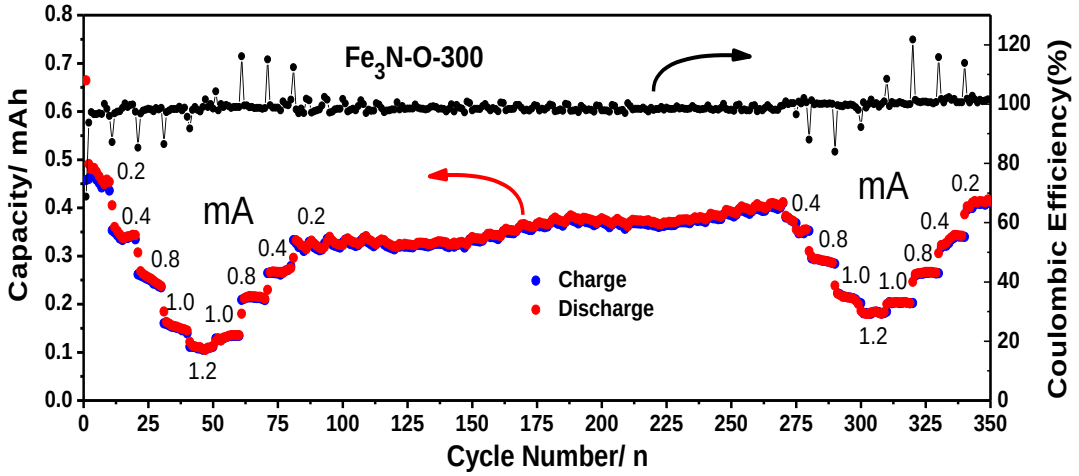

Figure 6. Rate performance, cyclic behavior and Coulombic efficiency of the Fe_3N-O sample

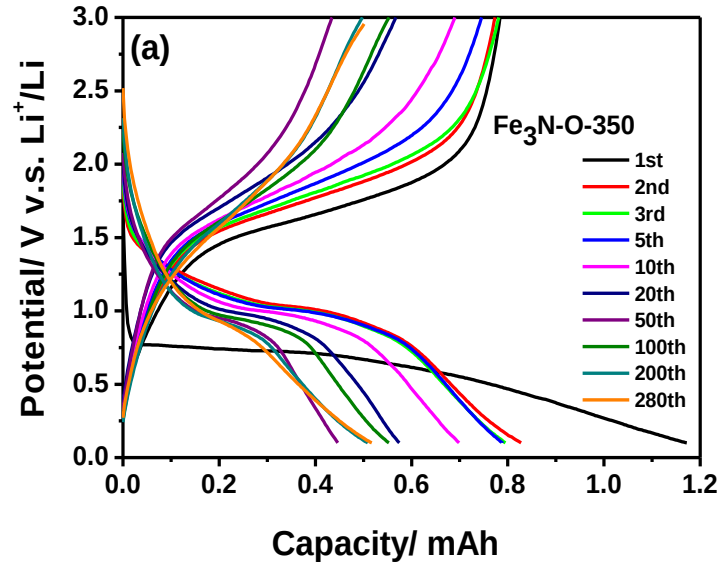

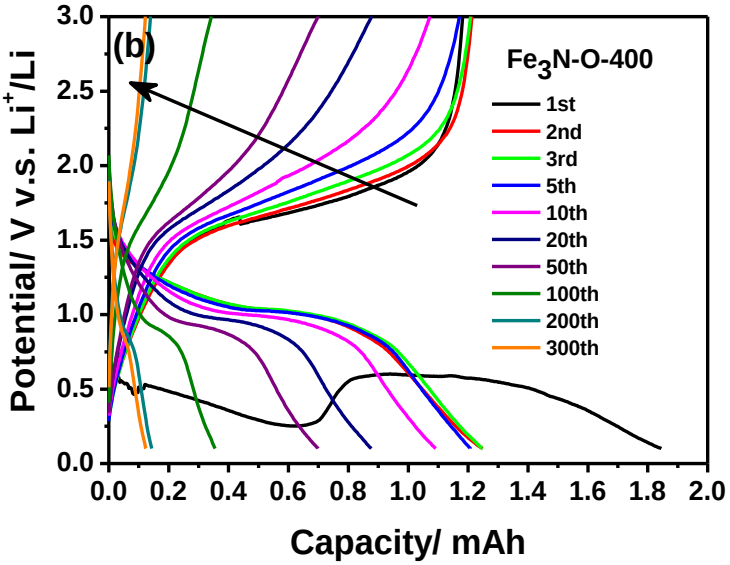

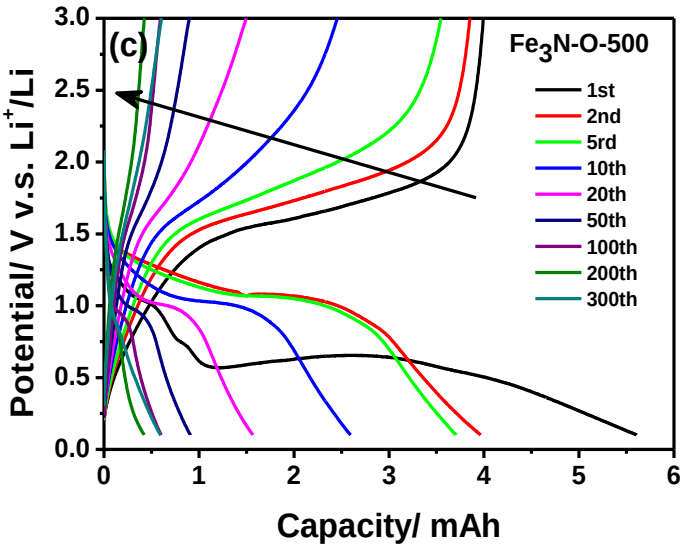

Figure 7. Discharge-charge voltage profiles of (a) Fe_3N-O-350, (b) Fe_3N-O-400, (c) Fe_3N-O-500

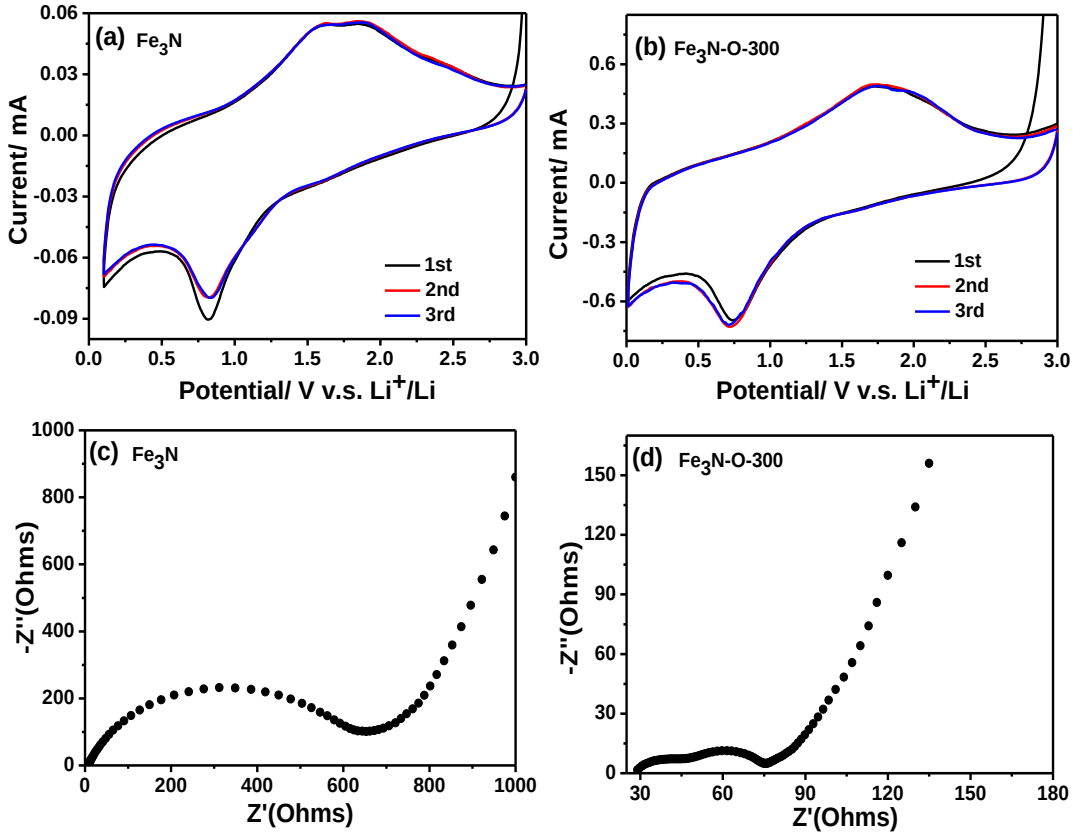

Figure 8. (a), (b) Cyclic voltammograms and (c), (d) Nyquist plots of the Fe_3N and Fe_3N-O-300 samples, respectively

The effect of oxidation temperatures on the capacity retention is shown in Fig. 7. Over 400 ^{o}C, the rapid capacity attenuation is observed from Fig. 7 b and c, similarly to that of Fe-O-400, although there is the interface of Fe_3N and Fe_3O_4-Fe_2O_3 according to the XRD data.

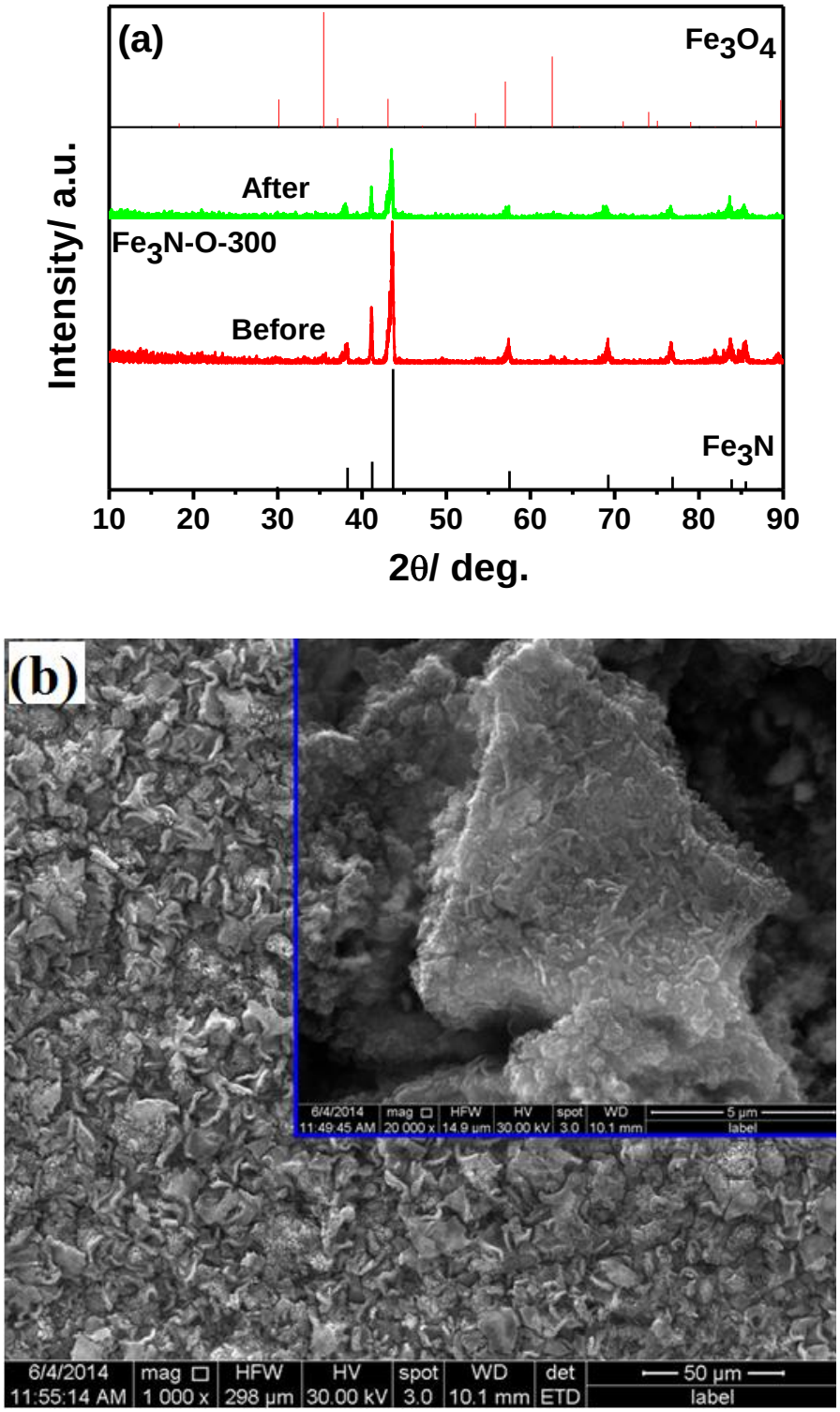

Figure 9. (a) XRD pattern and (b) SEM image of the Fe_3N-O-300 sample in charge state after 50 discharge/charge cycles

The crystal shape change and glass-like splinters formation, which are observed from the SEM images shown in Fig. 4, may be responsible for the irreversible capacity loss. At 350 ^{o}C, the capacity attenuation become weak, and after the 100th cycle the discharge-charge capacities increase.

The first three cyclic voltammograms (CVs) of the Fe_3N and Fe_3N-O-300 samples were measured between 3.00 and 0.01 V at a scan rate of 0.5 mV s^{-1}, after they underwent 50 discharge/charge cycles. The data are shown in Fig. 8 a and b, respectively. The clear cathodic peaks of the Fe_3N and Fe_3N-O-300 samples are observed at potentials of 0.82 and 0.73 V, respectively. However, from Fig. 8 a, two overlap anodic peaks can be distinguished, locating at 1.60 and 1.91 V. The result suggests that there a two-step anodic process for the Fe_3N electrode. While only a wide anodic peak is distinguished from Fig. 8 b, implying a one-step anodic process for the Fe_3N-O-300 electrode. Comparing with the two-group CVs, the cathodic/anodic currents of the Fe_3N-O-300 are far bigger than these of Fe_3N, indicating the Fe_3N-O-300 sample possesses higher electrochemical activation. Hence, The Fe_3N-O-300 material can release more capacity as shown in Fig. 5.

The distinct different between two Nyquist plots of the Fe_3N and Fe_3N-O-300 samples is that two depressed semicircles are observed from Fig. 8 d. But no two-semicircle phenomenon was observed from nanostructured iron oxides and the composites of iron oxides and carbon materials [13, 15]. The result suggests that besides one electrode-electrolyte interface there is the other interface, which should be the Fe_3N/Fe_3O_4 interface. The interface charge transfer resistance can be estimated to about 20 Ω (for 2 cm^2) from the EIS. Such an interface should be responsible for good electrochemical performances. Hence, when the Fe_3O_4-Fe_2O_3 layer become thick, which formed at a high temperature (for example 400 ^{o}C), a capacity loss with cycles can be observed due to weakening the interface effect.

The morphology and structure of the Fe_3N-O-300 sample in charge state were characterized after 100 discharge/charge cycles. As shown in Fig. 9 a, the main phase is still Fe_3N, however, all diffraction peaks became weak proportionally, implying that the Fe_3N was coated again by forming SEI and changing surface structure. At the same time, the original weak diffraction peaks of Fe_3O_4 are hardly observed after cycling, likely due to again spreading oxides on the Fe_3N reconstituting surface. Hence, as shown in Fig. 9 b the morphology changes seriously. The polygonal crystals disappear completely, for which irregular particles and sheets substitute. The morphology variation has been also observed in many redox-type electrodes [25, 26]. The structures consisted of micronparticles and micronsheets increase the interface surface between Fe_3N and iron oxides, consequently increasing the capacity retention.

4. CONCLUSION

A Fe_3N material contained of polygonal crystals with micro-pores was prepared by nitriding on the electrodeposited Fe disks. Then, the interface of Fe_3N and Fe_3O_4-Fe_2O_3 on the polygonal crystal surface was constructed by a simple oxidation of Fe_3N in air at 300 ^{o}C. But the polygonal structure was destroyed in air above 350 ^{o}C. The EIS with two depressed semicircles verified the existence of the

Fe_3O_4-Fe_2O_3/Fe_3N interface. The Fe_3N-O-300 sample oxidized at 300 ^oC exhibited good capacity retention of 83.67 % and a reversible capacity of 0.41 mA h after 350 cycling at different currents.

ACKNOWLEDGMENTS
This work was financially supported by the National Natural Science Foundation of China (51062018, 51262031), the Natural Science Foundation of Yunnan (2010FXW004), Program for Innovative Research Team (in Science and Technology) in University of Yunnan Province (2010UY08, 2011UY09), Yunnan Provincial Innovation Team (2011HC008), and the Education Department foundation of Yunnan Province (2013J006).

References

1. M. Ebner, F. Marone, M. Stampanoni, V. Wood, *Science*, 342 (2013) 716.
2. A. Ito, L. Zhao, S. Okada, J. Yamaki, *J. Power Sources.*, 196 (2011) 8154.
3. Y. Piao, H. S. Kim, Y. E. Sung, T. Hyeon, *Chem. Commun.*, 46 (2010) 118.
4. J. S. Chen, T. Zhu, X.H. Yang, H. G. Yang, X. W. Lou, *J. Am. Chem. Soc.*, 132 (2010) 13162.
5. W. Zhang, X. Wang, H. Zhou, J. Chen, X. Zhang, *J. Alloys Compd.*, 521 (2012) 39.
6. Q. Q. Xiong, Y. Lu, X. L. Wang, C. D. Gu, Y. Q. Qiao, J. P. Tu, *J. Alloys Compd.*, 536 (2012) 219.
7. X. L. Yu, S. R. Tong, M. F. Ge, J. C. Zuo, C. Y. Cao, W. G. Song, *J. Mater. Chem. A.*, 1 (2013) 959.
8. T. Zhu, J. S. Chen, X. W. Lou, *J. Phys. Chem. C*, 115 (2011) 9814.
9. L. Ji, Z. Tan, T. R. Kuykendall, S. Aloni, S. Xun, E. Lin, V. Battaglia, Y. Zhang, *Phys. Chem. Chem. Phys.*, 13 (2011) 7170.
10. D. Q. Liu, X. Wang, X. B. Wang, W. Tian, J. W. Liu, C. Zhi, D. He, Y. Bando, D. Golberg, *J. Mater. Chem. A.*, 1 (2013) 1952
11. Z. M. Cui, L. Y. Jiang, W. G. Song, Y. G. Guo, *Chem. Mater.*, 21 (2009) 1162.
12. F. Wu, R. Huang, D. B. Mu, X. Y. Shen, B. R. Wu, *J. Alloys Compd.*, 585 (2014) 783.
13. Z. P. Zeng, H. L. Zhao, J. Wang, P. P. Lv, T. H. Zhang, Q. Xia, *J. Power Sources.*, 248 (2014) 15.
14. P. Y. Li, J. C. Deng, Y. Li, W. Liang, K. Wang, L. T. Kang, S. Z. Zeng, S. H. Yin, Z. G. Zhao, X. G. Liu, Y. Z. Yang, F. Gao, *J. Alloys Compd.*, 590 (2014) 318.
15. R. Wang, C. Xu, J. Sun, L. Gao, C. Lin, *J. Mater. Chem. A.*, 1 (2013) 1794.
16. M. X. Gao, P. Zhou, P. Wang, J. H. Wang, C. Liang, J. L. Zhang, Y. F. Liu, *J. Alloys Compd.*,565 (2013) 97.
17. J. Su, M. Cao, L. Ren, C. Hu, *J. Phys. Chem. C.*, 115 (2011) 14469.
18. T. Yoon, C. Chae, Y. K. Sun, X. Zhao, H. H. Kung, J. K. Lee, *J. Mater. Chem.*, 21 (2011) 17325.
19. E. Kang, Y. S. Jung, A. S. Cavanagh, G. H. Kim, S. M. George, A. C. Dillon, J. K. Kim, J. Lee, *Adv. Funct. Mater.*, 21 (2011) 2430.
20. Y, B. Li, Y. R. Yan, H. Ming, J. W. Zheng, *Appl. Surf. Sci.*, 305 (2014) 683.
21. C. W. Su, W. Yang, J. M. Guo, Y. J. Zhang, *Vacuum.*, 86 (2012) 2095.
22. Z. W. Fu, Y. Wang, X. L. Yue, S. L. Zhao, and Q. Z. Qin, *J. Phys. Chem. B.*, 108 (2004) 2236.
23. L. Wang, L. Zhuo, C. Zhang, F. Zhao, *Chem. Eur.*, J. 20 (2014) 4308.
24. H. Wu, N. Du, J. Z. Wang, H. Zhang, D. R. Yang, *J. Power Sources.*, 246 (2014) 198.
25. C. W. Su, J. M. Li, W. Yang, J. M. Guo, *J. Phys. Chem. C.*, 118 (2014) 767.
26. S. Ni, X. Lv, T. Li, X. Yang, L. Zhang, Y. Ren, *Electrochim. Acta.*, 96 (2013) 253.